Journal of Power Sources 208 (2012) 248–256

Contents lists available at SciVerse ScienceDirect

Journal of Power Sources

journal homepage: www.elsevier.com/locate/jpowsour

Experimental investigation of water droplet emergence in a model polymer electrolyte membrane fuel cell microchannel

T.C. Wu, N. Djilali*

Institute for Integrated Energy Systems and Department of Mechanical Engineering, University of Victoria, Victoria, BC V8W 3P6, Canada

ARTICLE INFO

Article history:
Received 4 November 2011
Received in revised form 8 February 2012
Accepted 11 February 2012
Available online 19 February 2012

Keywords:
PEM fuel cell
Water management
Two-phase flow
Multiphase flow
Droplet dynamics
Contact angle hysteresis

ABSTRACT

Using quantitative flow visualization and a transparent microfluidic platform replicating the salient features of the cathode channel of a polymer electrolyte membrane fuel cell (PEMFC), we investigate the dynamic evolution of water droplets emerging from a single 50 μm pore of a gas diffusion layer (GDL) into a 250 μm × 250 μm air channel. The flow regimes are found to be primarily dependent on the air flow Reynolds numbers which ranged from 50 to 1200. At low Re, slug flow blocks the air flow through the channel. At higher Re, a periodic pattern of droplet emergence, growth and detachment appears. Further increase in air velocity induce wavy water film pattern. The characteristic frequencies and a flow map of the flow regimes as a function of superficial air and water velocities and presented. The significantly higher critical air velocities compared to previous results in the literature highlight the important impact of pore connectivity.

Three different phases are identified in the dynamic evolution of the contact angles in the droplet regime. Both advancing and receding angles initially increase at the same rate; in the next phase only the advancing angle increases; and finally both angles increase monotonically under the combined effect of pressure and shear forces, resulting in a maximum hysteresis of ∼110°. A decrease in the droplet aspect ratio (height to chord ratio) and contact angle hysteresis is observed in the film flow regime, and is found to reduce water removal capacity.

1. Introduction

Water management affects performance and durability of PEM fuel cells (PEMFCs), and remains a pacing item in the development of commercial stacks. In spite of a number of experimental and theoretical studies, the underlying liquid water transport, including water droplet generation, growth, detachment and removal processes, are not well understood. This stems from the modeling challenges associated with the complex dynamics of the two-phase flow, and from the optically inaccessible and electrochemically active nature of a fuel cell that make in situ measurements difficult. The experimental challenges and a review of the techniques used to date to visualize liquid water transport are discussed by Bazylak [1]. One of the most widely used approaches is optical visualization/photography in custom-designed transparent PEMFCs. This approach is exemplified by the work of Tüber et al. [2] who, based on their observations, concluded that hydrophilic diffusion layers resulted in increased current densities and better fuel cell performance as a result of more uniform membrane hydration. Yang et al. [3] visualized water droplet emergence from the GDL surface and its subsequent behavior in the gas channel. They found that droplets appear only at certain preferential locations, and can grow to a size comparable to the channel dimensions. A variety of phenomena in the gas channel were reported, including the intermittent emergence of droplets, film formation and channel clogging. Chen et al. [4] proposed a simplified force balance model based on droplet geometry approximations for predicting the onset of water droplet instability on GDL surfaces, and supported the model with experimental observations. They found that droplet removal can be enhanced by increasing the flow channel length or mean gas flow velocity, by decreasing the channel height or contact angle hysteresis (the difference between the advancing and receding contact angles), or by making the GDL more hydrophobic. Two different modes of liquid water removal were identified by Zhang et al. [5], and based on a further analysis using a force balance model, they proposed a relationship between the droplet detachment diameter and air velocity. Independently of Chen et al. [4], Kumbur et al. [6] conducted a similar theoretical and experimental study of the influence of controllable engineering parameters, including surface PTFE coverage, channel geometry, droplet chord dimensions, and operational air flow rate. The proposed water droplet instability criterion was formulated in terms of the Reynolds number and droplet aspect ratio. Theodorakakos et al. [7] constructed a platform consisting of a high

* Corresponding author. Tel.: +1 250 721 6034; fax: +1 250 721 6323.
E-mail address: ndjilali@uvic.ca (N. Djilali).

0378-7753/$ – see front matter © 2012 Elsevier B.V. All rights reserved.
doi:10.1016/j.jpowsour.2012.02.026

aspect ratio channel (2.7 mm × 7.0 mm) for visualizing the behavior of a single droplet placed on the surface of different GDLs. They obtained side-view droplet detachment images and measured the dynamic contact angles for input into their in-house volume-of-fluid (VOF) computer simulations, and were able to correlate the critical droplet diameter at detachment with the air velocity. The channel dimensions in these studies [6,7] were significantly larger than PEMFC gas flow channels, which have hydraulic diameters ranging from 200 μm to 3 mm [8], and though valuable, the insights from these studies are expected to have limited relevance to PEMFCs because of the important impact of reduced dimensions on the two-phase flow. Whereas previous experimental studies [2–7] investigated water droplets or films initially resting on a GDL, the actual water transport process in a PEMFC channel also involves the initial emergence of droplets into the GDL, their subsequent growth and detachment from the GDL and, finally, their interaction with the walls leading to a complex two-phase flow regime throughout the channel. The resulting flow regimes may vary between surface tension dominated slug flow and inertia dominated annular flow depending on the load [8]. The annular or dispersed droplet flow regime is desirable in fuel cell operation since this provides a path for reactant flow in the presence of water. However, due to the operational load of fuel cell stacks, the flow regime is at times likely to shift to slug flow because at low power the shear force in the cathode channels is usually insufficient to overcome the surface tension forces that hold water within the flow field channels and GDLs.

While microchannel two-phase flows have been the focus of many experimental and theoretical studies targeted at PEMFCs (see review by Anderson et al. [9]), such flows are also of relevant in applications ranging from heat sinks for electronic devices to microreactors and microfluidic devices. Most of the work in these latter applications is concerned with aqueous–aqueous systems, but a few studies have recently investigated gas–liquid systems using flow visualization and particle image velocimetry. Günther et al. [10] investigated different gas–liquid rectangular microfluidic channels and networks pertinent to chemical reactions and mapped bubbly, slug/plug and annular flow patterns as a function of the gas and liquid superficial velocities. A flow pattern map based on dimensional analysis and visualization was also presented by Waelchli and von Rohr [11] for conditions related to microreactors. Based on a critical review of available observations, it was noted that basing the similarity analysis on cross-sectional channel shape rather than hydraulic diameters is key for reliable prediction of flow regime based on experimental maps. This is consistent with the recent study of Kim et al. [12] who identified three fundamentally different two-phase flow regimes (capillary bubbly, segmented, annular) together with two transitory ones. They reported that the transition boundaries depend on the geometry of the test microchannels and of the injection port. They also noted differences in pressure drop for the capillary bubbly and segmented flow regimes when using different microchannel materials. These microfluidic studies were all performed using hydrophilic surfaces.

As in the case of microfluidic applications, two-phase flow regimes relevant to PEMFC cathodes can be broadly classified as slug, droplet and film flows, but the detailed characteristics and transition boundaries differ significantly due to the properties of the GDL, and particularly hydrophobicity and roughness. Each of the three regimes can occur solely in a channel, or two or more might occur simultaneously at different locations of the flow channel [9]. Hussaini and Wang [13] presented an in situ study of cathode flooding using a transparent PEMFC. Gas relative humidities of 26%, 42% and 66%, current densities of 0.2, 0.5 and 0.8 A cm^{-2} and flow stoichiometries ranging from 2 to 4 were used to represent typical operating conditions for automotive applications. Based on observed flow patterns and the superficial phase velocities, a flow map was developed and utilized to determine operating conditions that prevent channel flooding. However, there are inconsistencies in the observed flow patterns from various studies. Direct ex situ visualization of droplet evolution using laboratory models of fuel cell microchannels has allowed some detailed analysis not possible in situ. Hidrovo et al. [14] investigated water slug detachment in two-phase hydrophobic microchannel flows. Due to the aspect ratio and geometry of the microchannel water was observed to form pancake-like slugs rather than a spherical cap droplet. More recently, Lu et al. [15,16] presented flow visualization and pressure drop measurements over a broad range of flow regimes, flow parameters, channel surface wettability, geometry and orientation. Colosqui et al. [17] used an experimental set-up conceptually similar to the present one but with larger channel cross-sections in which gravity and surface tension forces are of the same order. Results showed that flow channel geometry and interfacial forces are the dominant factors in determining the size of slugs and the required pressure drop for their removal, and that residual water droplets can alter the wetting properties and act as a nucleating agents that impact the dynamics of slug formation and detachment. The interaction between the air and water flows that occur at the gas–liquid interface of a droplet was examined by Minor et al. [18]. Using micro-digital-particle-image-velocimetry (micro-DPIV) and examining seeded droplets first placed on a GDL, they analyzed the relationship between air velocity in the channel, secondary rotational flow inside a droplet, droplet deformation and contact angle hysteresis.

Computational analyses using model fuel cell geometries include previous work by our group [19] conducted using the volume-of-fluid (VOF) method. The formation of water droplets emerging through a micro-pore on a hydrophobic surface and its subsequent detachment and motion when subjected to air flow was simulated. It was found that the connection of the water droplet to the pore, and the emergence process has a very strong impact on the subsequent droplet dynamics. The critical air velocity for droplet detachment was found to be notably higher when droplet emergence is accounted for than when the droplets are initially assumed to be resting on the surface. Due to the small dimensions of the microchannel and the correspondingly high ratio of surface-to-volume forces, surface tension forces play an important role in determining water droplet dynamics. Surface forces acting at the phase boundaries are especially important. To improve the physics of VOF simulations such as those of Zhu et al. [19], data and suitable models are required for the dynamic contact angle and associated hysteresis.

Volume-of-fluid (VOF) CFD simulations performed to date by Zhu et al. [19] and others to investigate the dynamics of liquid water droplets in hydrophobic microchannels do not rigorously account for the moving contact line mechanisms and associated hysteresis, which in any case are not fully understood [20]. Computationally tractable dynamic VOF models proposed to date are based on semi-empirical prescriptions such as the Hoffman function [21]. Hao and Cheng [22] used a Lattice Boltzmann Method (LBM) with a multiphase free energy model to simulate a similar case to that of Zhu et al. [19] and capture the dynamic behavior of water droplets. Their simulations showed that water droplet removal is facilitated by a high gas flow velocity on a more hydrophobic GDL surface, and that water droplets lift off the surface for a highly hydrophobic surface.

Strategies for effective water management rely on an understanding of two-phase flow in gas channels in PEMFCs under realistic operating conditions. Since the primary source of the liquid phase in the gas channel is the water droplet transfer through the GDL, the analysis of water droplet development, evolution and instability behavior on the GDL surface is essential. Building our preliminary experiments [23] and previous computational work [19], we present an experimental characterization for the

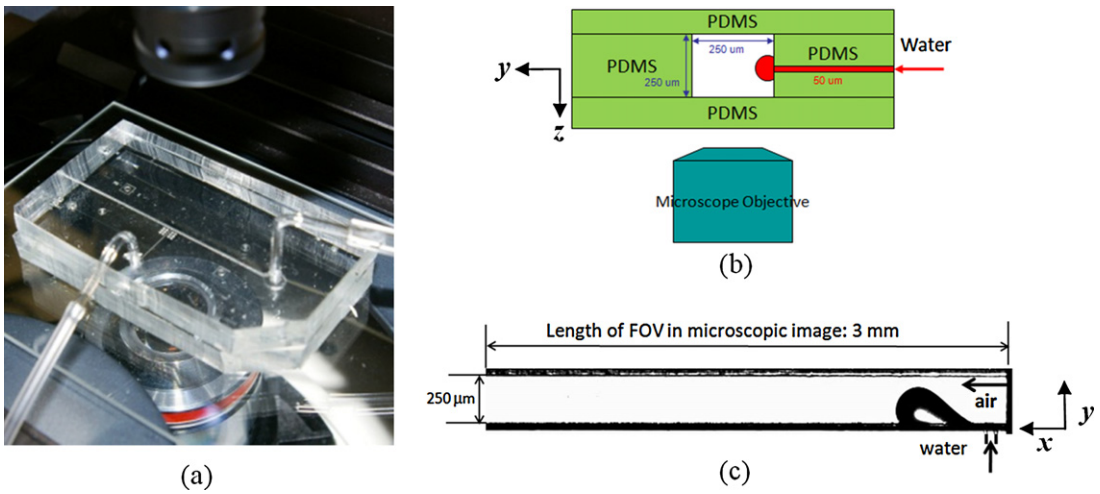

Fig. 1. PDMS chip for droplet manipulation, cross sectional view of chip, and field of view in microscope.

emergence, detachment and subsequent dynamic evolution of water droplets in laboratory model of a fuel cell cathode channel. The controlled ex situ experiments are analyzed using flow visualization and image analysis and provide further insight into the droplet dynamics process and quantitative data for the validation of numerical models.

2. Methods and apparatus

2.1. Microchannel design

A specifically designed microfluidics platform was fabricated for the experimental study of droplet dynamics. The water pore size and shape as well as the dimensions and surface properties of the microchannel must be considered in the design in order to model the phenomena of water emergence relevant to fuel cell operation. The microfluidic chip produced for this specific purpose (see Appendix for detailed fabrication procedure) includes a single channel with a cross section of 250 μm × 250 μm for air flow, as well as a single water injection pore with a cross section of 50 μm × 50 μm located in the middle of the air channel. An elastomer, polydimethylsiloxane (PDMS, Dow Corning Sylgard 184), was selected as the casting material not only due to its transparent and optical clear characteristic but also because its surface is hydrophobic and provides a static contact angle of ~110°, a value similar to that of carbon paper without PTFE coating.

For an actual GDL, pore sizes and locations are randomly distributed thus making it a challenge to predict and control the locations of water droplets in the fuel cells. However, the size of the "pores" is of the order of 50–100 μm [7]. Experimentally, the emergence pore location can be prescribed on a GDL as was also shown by Kimball et al. [24] by creating 250 μm pores at specific locations. There is also evidence that preferential pathways do form spontaneously in standard treated GDLs [25], probably as a result of residual water. In the present study, the 50 μm square size of water pore is prescribed to represent such conditions.

A complete chip is shown in Fig. 1a. Viewing from the side, Fig. 1b, allows observation of an emerging droplet as illustrated. The total length of the microchannel is around 37 mm, whereas the field of view of the microscopic images only covers 3 mm (Fig. 1c). The dimensions of the channel cross section are the same as reported by Zhu et al. [19], and are suitable for representing a typical gas flow channel used in micro PEM fuel cells [26]; the pore size for water emergence is close to the mean values for carbon paper reported in the literature [7,27]. Keeping in mind the intended use of the data for validation of various numerical methods [19,22,28], a square geometry was selected as it is computationally more convenient to reproduce without requiring grid skewing or unacceptable grid aspect ratios. The experimental set-up exhibits the most salient physical mechanisms and maintains the appropriate range of values for the key non-dimensional parameters.

Since gravity is perpendicular to the direction of water emergence, it is necessary to clarify the potential gravitational effects. The Bond number, denoted as the ratio of the gravitational force to the surface tension force, is defined as

$$Bo = \frac{\rho g L^2}{\sigma} \quad (1)$$

where ρ is the density of water droplet, g is the gravitational acceleration, L is the characteristic length of the system (the measured maximum droplet height is around 200 μm), and σ is the surface tension force between water and air. The Bond number in the current system is estimated to be less than 0.0054 indicating that surface tension forces dominate and the effects of gravity are negligible.

2.2. Measurement apparatus

A schematic diagram of the experimental apparatus is shown in Fig. 2. This setup allows injection of water from a small pore that emerges into an air stream while simultaneously monitoring the pressure drop across the gas channel (ΔP), the injected water volume (Q_w), and the air flow rate (Q_a). A side view visualization of two-phase flow is obtained as droplets move and interact with the gas stream inside the microchannel. The data acquisition system was developed using LabView 8.5 (National Instruments) to integrate the water syringe pump (Harvard Apparatus, PHD 2000), air mass flow meter (Omega, FMA-1600A), differential pressure sensor (Honeywell, FP2000), and high-speed camera (Vision Research, Phantom MIRO-4). Data streams are initialized by the high-speed camera to trigger the image sampling process. Eight-bit, gray scale images are captured as well as time-resolved pressure drops, delivered water volumes, air flow rates, and inlet upstream pressures and temperatures. These can be measured simultaneously allowing correlation of droplet dynamics with flow regimes. The collected data provide initial conditions, making the experiments suitable for numerical validation. Digital image processing was performed using the toolbox in Matlab 7.8. Images were recorded

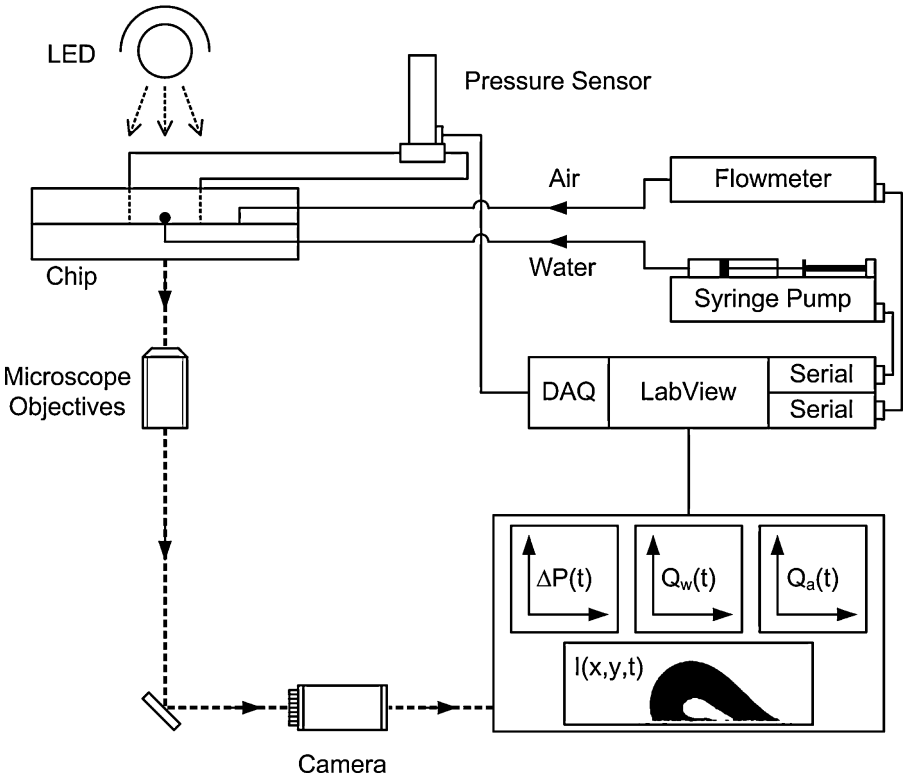

Fig. 2. Schematic diagram of experimental apparatus.

through an inverted microscope (Zeiss, Axiovert 200M) and magnified by a 5× objective lens (Zeiss, EC Plan Neofluar). Bright-field illumination using a white light LED was applied throughout the image acquisition process.

The high-speed camera consists of a CMOS (complementary metal oxide semiconductor) image sensor with a maximum of 800 × 600 pixels. It has a capability of 12-bit pixel depth and a maximum full-resolution frame rate of 1000 Hz. However, in order to resolve the droplet dynamics, the images were adjusted to covering only 800 × 72 pixels. This boosts the camera frame rate up to 6006 Hz and provides around 6 s of recording time with the 2GB built-in memory in the camera. Time resolved images were fed into the contact angle measurement software (DataPhysics Instruments, SCA202 v3.51.3 build 187). The tangent method for sessile drop measurement that fit the three-phase point where the liquid touches the solid surface was used. A third degree rational function was used to evaluate the advancing and receding contact angles as well as to measure the droplet height and chord length. The accuracy of the contact angle analysis depends upon the image processing technique and parameters used to extract the drop edge from images. Droplet images are converted into 8-bit gray scale by thresholding, resulting in images consisting of a dark foreground representing the drop, and a white background. When moving from the background into the droplet, a sharp decline in pixel intensity is observed, and the edge of the drop is expected to be in a region along the curve (spline) corresponding to the highest gradient. Using a maximum of 80 points to define the interface profile, a least square fit is used to determine the tangent at the advancing and receding contact points. The raw image from the high-speed camera provides a resolution of 4.54 μm per pixel. Due to the small droplet dimension (100–350 μm), the raw images are imported into the contact angle evaluation program after a three-fold magnification. Combining the uncertainties results in a maximum uncertainty of ±1.3°.

2.3. Flow conditions

The flow channel described in Section 2.1 (250 μm × 250 μm cross section and 37 mm length) nominally simulate an operating fuel cell active area (A_{act}) of 0.0925 cm^{-2}. The volumetric flow at the cathode due to water production and anode-to-cathode transport is given by:

$$Q_w = \frac{(1+2\alpha) i A_{act} M_{H_2O}}{2F} \quad (2)$$

where α is the net drag coefficient, A_{act} is the active area, i is the current density, M_{H_2O} is the molecular weight of water, and F is Faraday's constant. For operation at $i = 2.0\ A\,cm^{-2}$ with $\alpha = 1$, the water flux is 33.6 $\mu L\,min^{-1}\,cm^{-2}$. The injection rates used in this study range from 32.4 to 162.2 $\mu L\,min^{-1}\,cm^{-2}$. The higher water flow rate were specifically chosen to allow us to conduct the experiments in a reasonable time and without incurring secondary effects such as evaporation. Appropriate normalization of the time scale and the negligible impact of water injection rates on contact angles and droplet dimensions discussed in the results below support this. The Reynolds numbers for the air flow range from approx. 50 to 1200, representative of a range of operating conditions for parallel and serpentine PEMFC configurations. The inlet flow conditions used in the experiment are summarized in Table 1.

3. Results and discussions

The flow visualization experiments were analyzed both qualitatively, to develop a flow regime map, and quantitatively, to determine the evolution of the dynamic contact angle, the characteristic detachment frequency and droplet size.

Table 1
Flow inlet conditions.

Test matrix for flow regime	
Air flow rate, Q_a (sccm)	12–300
Air superficial velocity, V_a (m s^{-1})	3.2–80
Water flow rate, Q_w (μL min^{-1})	3, 6, 15
Water superficial velocity, V_w (m s^{-1})	0.02, 0.04, 0.10
Reynolds number of air, Re	51–1268
Temperature, T (K)	296

Two specific cases for qualitative droplet dynamic analysis, Case 1: $V_a = 10$ m s^{-1}, $V_w = 0.02$ m s^{-1} and Case 2: $V_a = 10$ m s^{-1}, $V_w = 0.04$ m s^{-1}.

3.1. Flow regimes

In order to investigate the water droplet dynamics subjected to a shear flow in the microchannel corresponding to a range of fuel cell operating conditions, three water superficial velocity conditions were investigated. The superficial velocity is defined as the bulk velocity of the water flowing through the cross sectional area of the channel. Visualization of the water emergence process could be typically categorized into three distinct flow regimes shown in Fig. 3:

1. *Slug flow* (Fig. 3a) occurring at low air superficial velocities. The drag force is minimal at these velocities, and the droplets keep growing until they contact the channel wall and are then either slowly convected or remain on the wall until caught up by another droplet with which they coalesce and then move along the channel toward the outlet. Slug flow obstructs and limits air flow through the channel and thus increases the possibility of flooding and decreases the water removal effectiveness in the channel.
2. *Droplet flow* (Fig. 3b) occurring at increasing air velocity, with an individual droplet emerging from the water pore and remaining pinned at the water pore due to surface tension forces, until it grows to a critical size at which the air drag force overcomes the surface tension force. In this regime, the effect of air velocity on the changing shape of the emerging droplet and the time evolution of the emerging process can be clearly identified.
3. *Film flow* (Fig. 3c) that ensues with further increase in air flow velocities that drag the droplets and induce the formation of an elongated and almost continuous wavy water film. Large droplets are no longer observed. Instead, smaller protrusions appear at the boundary of the film and are rapidly flattened due to a high air flow rate.

In summary, the water droplets can be shearing off the PDMS surface with a higher air flow velocity, causing only a minimal obstruction. This occurs most often while droplets are small compared with the channel geometry. Upon detachment, the droplet can interact with the different channel walls. The detached water droplets can adhere to the surfaces, coalesce and build up into water lumps, films or slugs, blocking the flow passage over time. The different coalesced structures of water inside the flow channel will produce different flow instabilities.

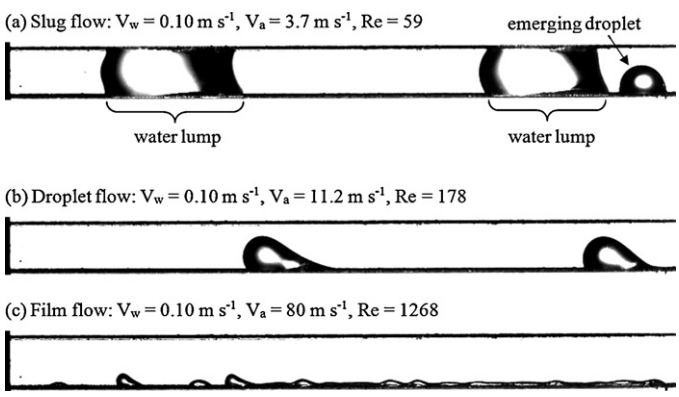

Fig. 3. Typical two-phase flow regime in microchannel.

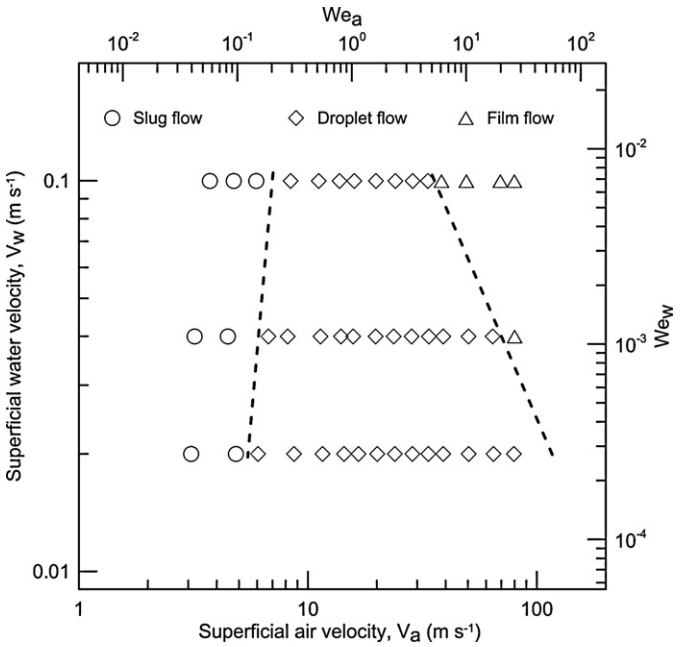

Fig. 4. Flow map of water emergence phenomena in a model PEMFC cathode gas microchannel.

The different flow regimes are typically presented in two dimensional flow pattern maps, with the two coordinates representing some appropriate hydrodynamic parameters. The most popular coordinates are superficial phase velocities, but dimensionless Weber numbers have also been used, as suggested by Akbar et al. [29]. Both representations are shown in Fig. 4. Dashed lines are used to delineate the three different regimes based on the testing conditions, and provide the threshold air velocities for the transitions from slug flow to droplet flow and then to film flow at a given water velocity. With increasing water velocity, the droplet flow regime region becomes smaller, and at some point the slug and film regimes intersect, with transition occurring directly and bypassing the droplet flow regime.

3.2. Droplet emergence frequency

The flow visualization presented above indicates that the periodicity of the droplet emergence process is specific to the flow regime. Time series analysis was performed to further characterize the droplet dynamics using digital imaging processing. Time series raw images are first subtracted from a reference background image taken in the absence of droplets. All images are cropped to the region of interest covering a single droplet in a preselected registered image. This registered image is then compared with other images by using a MATLAB image processing and signal analysis toolbox. Preselected registered image A is compared with every other image B in the same recording series. An algorithm to determine the two-dimensional correlation coefficient index, r, is applied based on

$$r = \frac{\sum_m \sum_n (A_{mn} - \bar{A})(B_{mn} - \bar{B})}{\sqrt{\left(\sum_m \sum_n (A_{mn} - \bar{A})^2\right)\left(\sum_m \sum_n (B_{mn} - \bar{B})^2\right)}} \quad (3)$$

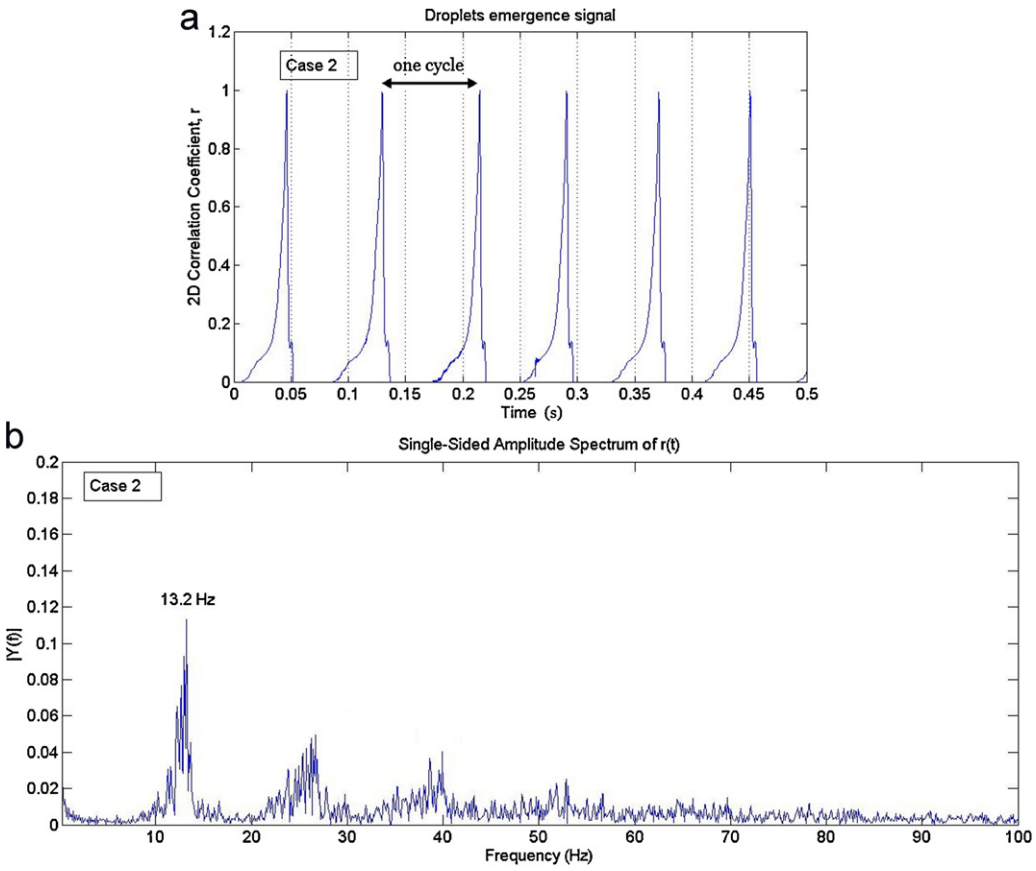

Fig. 5. (a) Time domain signal and (b) frequency distribution of droplet emergence process.

where A_{mn} and B_{mn} are $m \times n$ matrices, and $\bar{A}$ and $\bar{B}$ are the mean matrix elements. The correlation coefficient values range from 0 to 1. When using the algorithm to compute time resolved image correlations, a few images are randomly selected to serve as the register image A, and are compared with image B in the image stack. The two experimental flow conditions listed in Table 1 were selected to demonstrate the concept.

A typical time domain signal for Case 2 is shown in Fig. 5a and the corresponding frequency spectrum obtained using a Fast Fourier Transform (FFT) analysis is shown in Fig. 5b, clearly identifying the periodicity. In Case 2, the droplet emerges at a dominant frequency of 13.2 Hz. The evolution of the dominant emergence frequency with flow conditions is presented in Fig. 6. The low emergence frequency at low air velocities allows droplets to grow sufficiently large to contact the side walls. The frequency increases linearly with air velocity and reaches its highest value before transitions to film flow. No dominant frequency is observed in the film flow regime, where the process is inherently a periodic due changes in detachment frequency and necking, splitting and coalescence of the films. The volume of a droplet can be further deduced from the water flow rate and the emergence frequency. In the current studies, the droplet volumes reached up to the onset of detachment range from 4.2 to 10 nL, 1.1 to 10 nL and 0.7 to 2.5 nL for water flow rates of 0.02, 0.04 and 0.1 μL min^{-1}, respectively. Interestingly, this suggests that this chip platform is promising for manipulation of a nanoliter droplet.

3.3. Further image analysis of droplet emergence

Fig. 7 displays time series images captured at 6006 Hz illustrating the evolution and cyclic nature of the water emergence into the gas stream. Only one cycle of emergence is shown corresponding to Case 2. The emergence frequency is 13.2 Hz (with a period of 75.75 ms), as presented earlier. The right boundary of the droplet is pinned at the water outlet where the air, water and the PDMS surface meet. The dynamics of a droplet is governed by the balance of pressure, shear and drag forces exerted on it. Surface forces dominate the beginning of the growth and emergence cycle (0–10 ms)

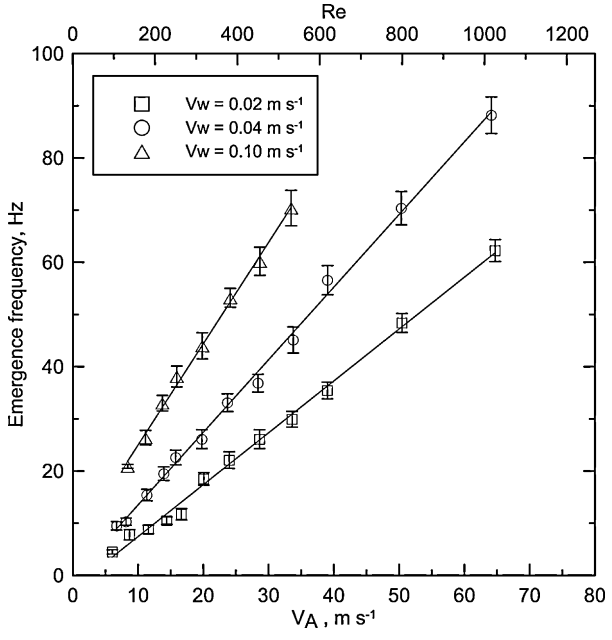

Fig. 6. Emergence frequency in droplet flow regime under different flow conditions.

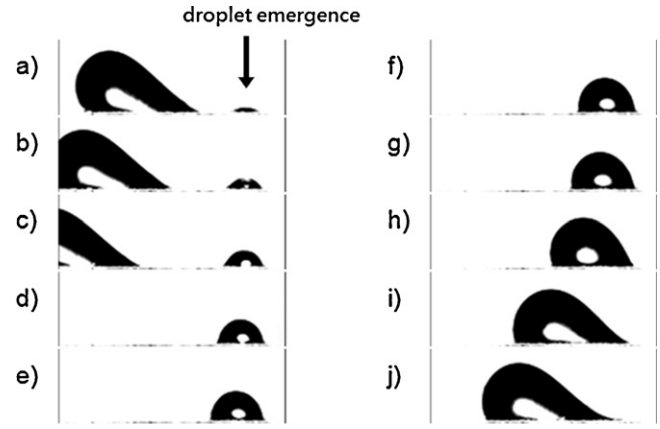

Fig. 7. Time resolved images of water emerging from a 50 μm square pore in a 250 μm square gas microchannel with the flow condition of Case 2: (a) t = 1 ms, (b) t = 3 ms, (c) t = 5 ms, (d) t = 10 ms, (e) t = 15 ms, (f) t = 20 ms, (g) t = 25 ms, (h) t = 45 ms, (i) t = 65 ms, (j) t = 75 ms.

shown in Fig. 7a–d during which the droplet retains a symmetric shape. Starting with Fig. 7e, the larger droplet produces increasing blockage of the air flow that results in increasing drag force inducing deformation with tilting toward the downstream direction and the onset of contact angle hysteresis. However, the surface adhesion forces still dominate drag and the droplet remains pinned. For these flow conditions, the droplet does not grow sufficiently large to contact the top and side walls, but eventually detaches (Fig. 7j) and starts to move along the surface while another emergence cycle begins.

3.4. Dynamic contact angle

The high-speed visualization images were further analyzed frame by frame to deduce the evolution of the droplet chord and height and of the dynamic contact angles. The advancing (θ_a, upstream de-wetting side) and receding (θ_r, downstream wetting side) contact angles of a droplet vary from the static value as shown schematically in Fig. 8a, and their evolution during the emergence process up to the point of detachment is presented in Fig. 8b for Case 2. Three different periods can be identified. Period I (0–11 ms: surface tension dominated) corresponds to the beginning of emergence. In this region, θ_a and θ_r increase at the same rate which corresponds to a symmetric change of the droplet shape and thus no contact angle hysteresis is observed. In Period II (11–17 ms: transient region), θ_a keeps increasing but θ_r stops increasing. This occurs as a result of pressure forces acting on the upstream surface of the droplet and countering the increase in θ_r due to droplet growth. In Period III (17–75.75 ms) increasing pressure and shear forces combined with growth induce further increase in the advancing contact angle θ_a up to 110°. During this process, significant distortion of the droplet occurs. Conversely, the receding contact angle becomes smaller as the cycle progresses up to detachment. The small variations in measurements around the trend lines are due to local variations in the PDMS surface of each batch of fabricated chips. Additionally the experimental surfaces are not perfectly homogeneous and occasional slip, jump and stick motion of the contact line were observed in flow visualization using a high-speed camera. These phenomena are expected to be more pronounced in actual GDL, in which is likely to play an even more prominent role.

The chord length of a growing droplet increases and reaches about 350 μm at detachment which is larger than the channel dimension of 250 μm. This underscores the significant deformation and elongation due to the hydrodynamic forces exerted by the

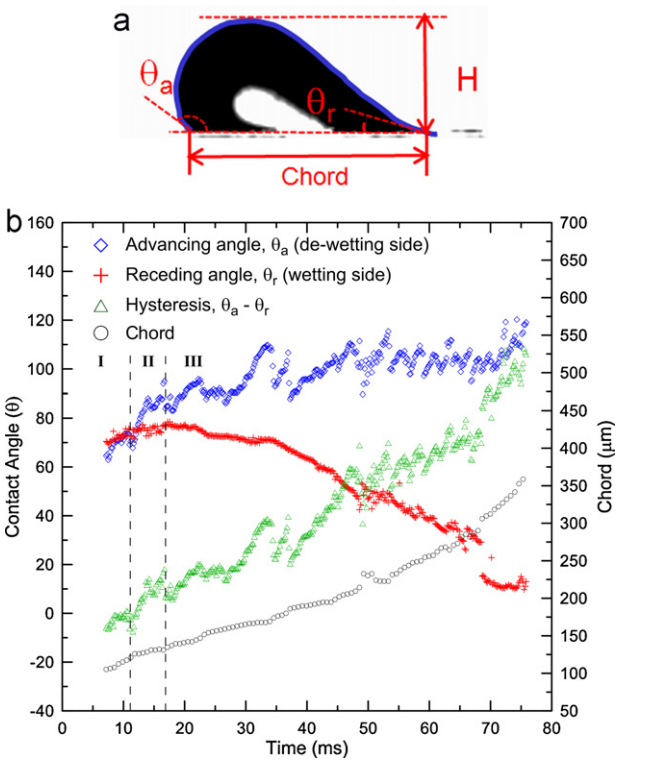

Fig. 8. Dynamic contact angle evolution through an emergence cycle (13.2 Hz under Case 2 flow condition).

air stream. The assumption of a spherical droplet in the simplified models for predicting the onset of droplet instability [4] are thus only very approximate. The data presented here for the time evolution of the dynamic contact angles can be used to empirically prescribe the dynamic contact angle in order to improve the physical realism of simulation.

3.5. Droplet dynamics at the onset of detachment

When water is introduced into the air stream, the droplet initially emerges, grows and remains pinned at the pore until it attains a critical size and detaches. The detachment droplet size is a function of several parameters, including water and air flow rates surface conditions, and pore size [30]. The droplet chord length, height, and the advancing and receding contact angles can be deduced from the flow visualization at the onset of detachment. The dependence of the detachment droplet chord (C) and height (H) on air velocity/Reynolds number is plotted in Fig. 9 for various water injection velocities. The air velocities can be interpreted as the critical operating velocities which must be used in a PEMFC to ensure detachment and removal of liquid water to prevent flooding and the subsequent blockage of the transport of reactants to the reaction sites [31]. The windows in the figure delineate the size of droplet flow regime for three different water injection velocities. The left and right hand sides of the window represent slug and film flow regimes, respectively. The low velocity boundary of the windows at around V_a = 8 m s^{-1} can be interpreted as the threshold air velocity that prevents the formation of slug flow which is characterized by larger droplets and blockage. Slower water injection velocities broaden the droplet flow regime window. The figure also shows a similar trend to the numerical data presented by Zhu et al. [32] with the rate of size decrease tapering at higher velocities.

The effect of the air flow on contact angle hysteresis ($\Delta = \theta_a - \theta_r$) is plotted in Fig. 10. This angle could be interpreted as the measure of the ability of the droplet to resist the drag force and the capability

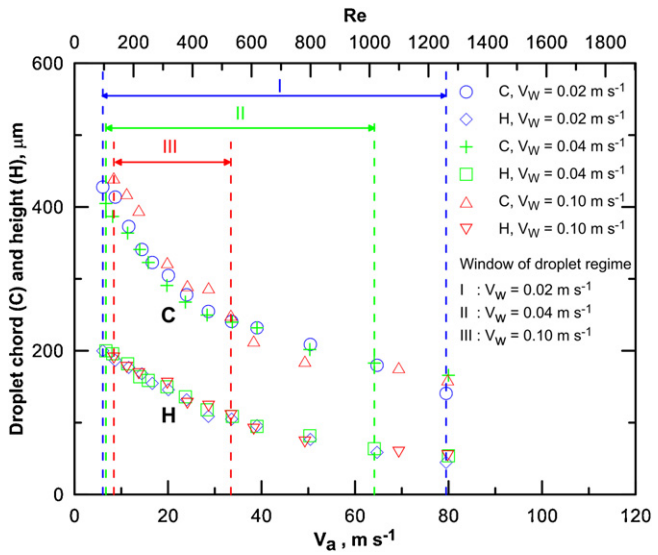

Fig. 9. Effect of air flow velocity on characteristic droplet size (chord C and height H) at detachment.

of the flat PDMS surface to remove water under controlled experimental conditions. The data for different water velocities collapses to the same curve and decreases linearly from 80° to 40°. As the air flow velocity increases, the flow regime changes from a droplet pattern to a film pattern with a smaller advancing contact angle and a reduction in the contact angle hysteresis. The analysis of Kumbur et al. [6] indicated that the contact angle hysteresis depends on the channel air flow rate (or Reynolds number), droplet size (H and C) and surface properties. The plot of the contact angle hysteresis versus the H/C ratio at different Reynolds numbers is shown in Fig. 11a. The data differs from that predicted by Kumbur et al. [6]. However, in their analysis, in addition to different flow conditions, the droplet was assumed to be hemispherical and symmetric and the effect of pore pinning was not accounted for. The importance of accounting for pore connectivity in determining the critical detachment size was highlighted by Zhu et al. [20]. The data obtained here reflects the distribution on a flat PDMS surface under flow

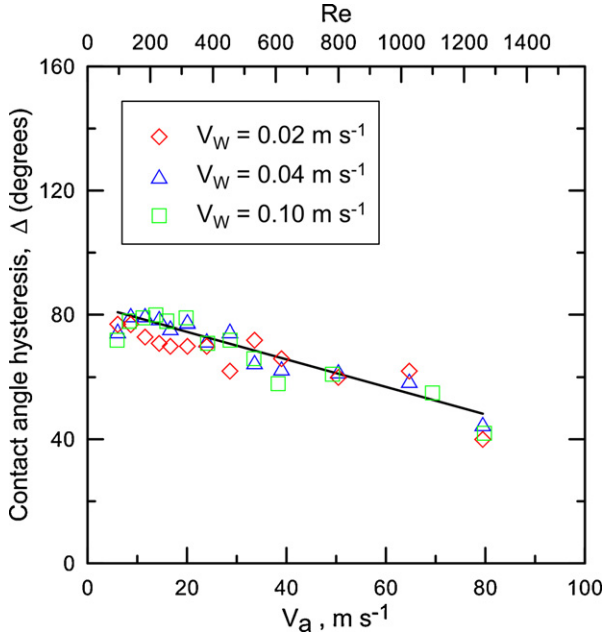

Fig. 10. Effect of air flow on contact angle hysteresis.

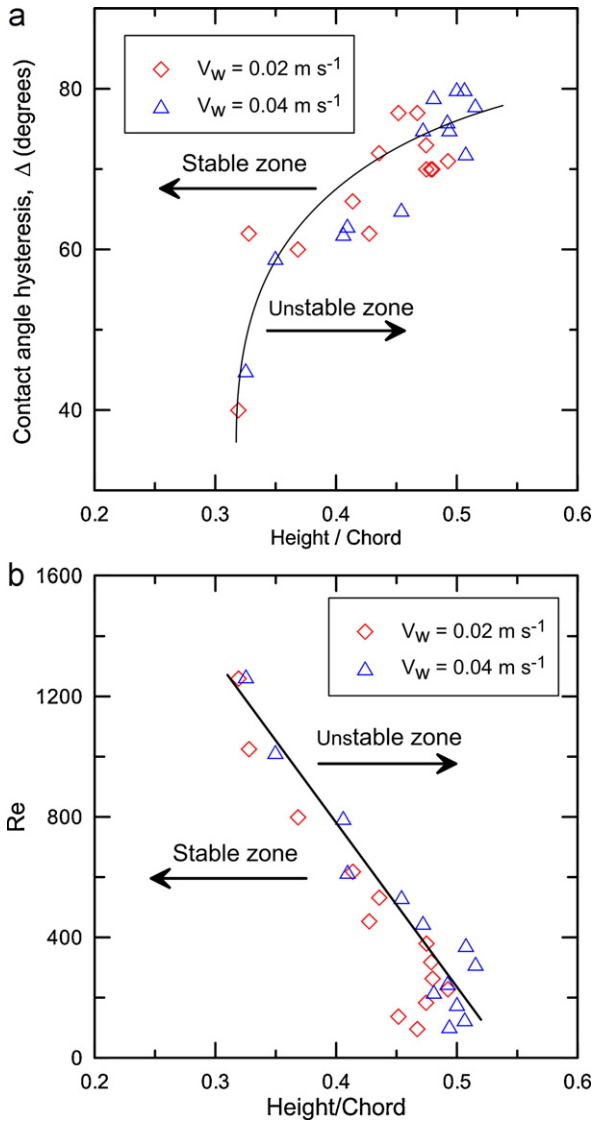

Fig. 11. Contact angle interpretations and effect of airflow on droplet aspect ratio at the onset of detachment.

conditions described in the test matrix of experiments. For a given droplet size (or aspect ratio, H/C), a higher contact angle hysteresis will increase the capability of the droplet to resist the drag force. The droplet will thus have a broader stability zone as shown by plotting the data appropriately in Fig. 11a. In fuel cell applications, a broader instability zone is desirable to enhance water removal capabilities. Fig. 11b shows the critical droplet size in terms of the aspect ratio versus the Reynolds number. A higher Reynolds numbers at a given droplet size increases instability and potential for removal of the droplet. The Reynolds number required to sweep out a droplet is found to increase with decreasing droplet aspect ratio. Spreading of the droplet, as discussed in [6], results in a decrease of the aspect ratio and requires higher air velocities/Reynolds number for detachment. As shown in the flow visualization, a decrease in the aspect ratio occurs when the flow regime switches to a film flow pattern. This flow regime makes water removal more difficult in fuel cell applications. Another parameter that impacts the droplet detachment process is pore diameter. Varying pore size was outside the scope of the present experiments, but numerical simulations [30] indicate that although the aspect ratio decreases with decreasing pore diameter, the critical Reynolds number for droplet removal decreases as a result of weaker surface tension due to the

reduced connectivity with the pore. The role of pore connectivity is clearly important and requires more in-depth analysis.

4. Conclusions

The dynamics of water droplets emerging from a pore in the presence of a cross flow of air was investigated experimentally using a modeled PEMFC cathode gas channel. Quantitative analysis of high-speed flow visualizations was performed to deduce characteristic process frequencies, contact angle hysteresis and critical droplet sizes. The study shows

1. Three flow regimes: slug, droplet and film flow patterns, are identified under different air and water velocities. At low air velocities, slug flow blocks the air flow through the channel. At higher air velocities, a periodic pattern of droplet emergence, growth and detachment appears. Further increase in air velocity induce wavy water film pattern. A flow map of the flow regimes as a function of superficial air and water velocities was presented.
2. For emerged droplets, significantly higher critical air velocities are observed compared to results in the literature which only considered processes starting from droplet initially static on a flat surface. This highlights the important impact of pore connectivity.
3. The dynamic contact angle at the onset of detachment decreases as the air velocity increases; as a result, the flow regime shifts from slug to droplet and film flow. This angle is representative of droplet stability, i.e. its ability to resist the drag force on a given surface.
4. A decrease in the droplet aspect ratio and contact angle hysteresis is observed in the film flow regime, and is found to reduce water removal capacity.

While the experiments presented here were obtained using a laboratory model of a PEMFC cathode, they isolate and represent some of the salient flow features of operating fuel cells, and the data and documented boundary conditions should prove useful for the validation of simulation methods. Two key characteristic of GDLs that will be considered in future work are roughness and inhomogeneities. These are expected to impact the effective contact angle, induce additional pinning and alter the droplet growth and dynamics. Finally, the critical impact of pore connectivity and pinning, which was also qualitatively reproduced in earlier numerical work [19], needs to be incorporated into practical force-balance models that can be used in design.

Acknowledgements

The authors would like to acknowledge the financial support from the Natural Sciences and Engineering Research Council of Canada, the Canada Research Chairs program, Ballard Power Systems and CFD Research Corporation.

Appendix A. Microfluidic chip fabrication

Chips incorporating the microchannels were fabricated on a 3″ silicon wafer by a sequential multi-layer SU-8 (MicroChem Corp.) fabrication process [33]. Two different high-resolution laser photo-plotted masks were prepared for the water and air delivery networks. A 25 μm layer of SU-8 25 was first spin coated, baked, exposed and developed to form the water delivery path. This process was repeated for a second 125 μm SU-8 100 layer to form the air delivery path. The finished multi-layer SU-8 structure served as the molding master for soft lithography techniques [34]. Two different mixture ratios of PDMS, 15:1 (with excess vinyl groups) and 5:1 (with excess Si–H groups), were cast separately on the multi-layer molding master and thermally cured on a hotplate at 80 °C for 40 min. The cured PDMS polymer was peeled off from the master mold, punched for fluidic access for water and air, diced, ethanol cleaned and finally air dried. The molding master was treated with a few drops of Repel-Silane ES (General Electric PlusOne) liquid for 5 min before each use for casting to prevent adhesion of the PDMS on the SU-8. Two symmetric elastomers with different mixture ratios of PDMS were carefully aligned to each other by predefined alignment marks under a stereo microscope providing ±5 μm precision. The aligned chip was thermal bonded on a hotplate at 80 °C for 2 h or overnight to increase the strong interfacial bonding between the two pieces. The secure bonding between the two pieces is important to prevent any leakage in the air stream at pressures up to 3 atmospheres. After bonding, a complete chip consists of a 50 μm square water pore and a 250 μm square air channel as shown in Fig. 1a.

References

[1] A. Bazylak, Int. J. Hydrogen Energy 34 (2009) 3845–3857.
[2] K. Tuber, D. Pocza, C. Hebling, J. Power Sources 124 (2003) 403–414.
[3] X.G. Yang, F.Y. Zhang, A.L. Lubawy, C.Y. Wang, Electrochem. Solid State Lett. 7 (2004) A408–A411.
[4] K.S. Chen, M.A. Hickner, D.R. Noble, Int. J. Energy Res. 29 (2005) 1113–1132.
[5] F.Y. Zhang, X.G. Yang, C.Y. Wang, J. Electrochem. Soc. 153 (2006) A225–A232.
[6] E.C. Kumbur, K.V. Sharp, M.M. Mench, J. Power Sources 161 (2006) 333–345.
[7] A. Theodorakakos, T. Ous, A. Gavaises, J.M. Nouri, N. Nikolopoulos, H. Yanagihara, J. Colloid Interface Sci. 300 (2006) 673–687.
[8] T.A. Trabold, Heat Transfer Eng. 26 (2005) 3–12.
[9] R. Anderson, L. Zhang, Y. Ding, M. Blanco, X. Bi, D.P. Wilkinson, J. Power Sources 195 (2010) 4531–4553.
[10] A. Gunther, S.A. Khan, M. Thalmann, F. Trachsel, K.F. Jensen, Lab Chip 4 (2004) 278–286.
[11] S. Waelchli, P.R. von Rohr, Int. J. Multiphase Flow 32 (2006) 791–806.
[12] N. Kim, E.T. Evans, D.S. Park, S.A. Soper, M.C. Murphy, D.E. Nikitopoulos, Exp. Fluids 51 (2011) 373–393.
[13] I.S. Hussaini, C.-Y. Wang, J. Power Sources 187 (2009) 444–451.
[14] C.H. Hidrovo, F.-M. Wang, J.E. Steinbrenner, E.S. Lee, S. Vigneron, C.-H. Cheng, J.K. Eaton, K.E. Goodson, ASME Conference Proceedings 2005, 2005, pp. 709–715.
[15] Z. Lu, S.G. Kandlikar, C. Rath, M. Grimm, W. Domigan, A.D. White, M. Hardbarger, J.P. Owejan, T.A. Trabold, Int. J. Hydrogen Energy 34 (2009) 3445–3456.
[16] Z.J. Lu, C. Rath, G.S. Zhang, S.G. Kandlikar, Int. J. Hydrogen Energy 36 (2011) 9864–9875.
[17] C.E. Colosqui, M.J. Cheah, I.G. Kevrekidis, J.B. Benziger, J. Power Sources 196 (2011) 10057–10068.
[18] G. Minor, N. Djilali, D. Sinton, P. Oshkai, Fluid Dyn. Res. 41 (2009) 045506.
[19] X. Zhu, P.C. Sui, N. Djilali, J. Power Sources 181 (2008) 101–115.
[20] B. Terence D, J. Colloid Interface Sci. 299 (2006) 1–13.
[21] S. Sikalo, H.D. Wilhelm, I.V. Roisman, S. Jakirlic, C. Tropea, Phys. Fluids 17 (2005) 062103.
[22] L. Hao, P. Cheng, J. Power Sources 190 (2009) 435–446.
[23] T.-C. Wu, N. Djilali, 20th International Symposium on Transport Phenomena, Victoria, BC, Canada, 2009.
[24] E. Kimball, T. Whitaker, Y.G. Kevrekidis, J.B. Benziger, AIChE J. 54 (2008) 1313–1332.
[25] A. Bazylak, D. Sinton, N. Djilali, J. Power Sources 176 (2008) 240–246.
[26] N.T. Nguyen, S.H. Chan, J. Micromech. Microeng. 16 (2006) R1–R12.
[27] S. Litster, D. Sinton, N. Djilali, J. Power Sources 154 (2006) 95–105.
[28] J. Choi, G. Son, J. Mech. Sci. Technol. 23 (2009) 1765–1772.
[29] M.K. Akbar, D.A. Plummer, S.M. Ghiaasiaan, Int. J. Multiphase Flow 29 (2003) 855–865.
[30] X. Zhu, P.C. Sui, N. Djilali, J. Power Sources 172 (2007) 287–295.
[31] T. Berning, N. Djilali, J. Electrochem. Soc. 150 (2003) A1589–A1598.
[32] X. Zhu, P.C. Sui, N. Djilali, Microfluid Nanofluid 4 (2008) 543–555.
[33] A. Mata, A.J. Fleischman, S. Roy, J. Micromech. Microeng. 16 (2006) 276–284.
[34] Y.N. Xia, G.M. Whitesides, Annu. Rev. Mater. Sci. 28 (1998) 153–184.